Universiteit Leiden
The Netherlands

Patient-specific in-vivo QA in MRGRT: 3D EPID dosimetry for the Unity MR-linac

Torres Xirau, I.

Citation

Torres Xirau, I. (2020, September 15). *Patient-specific in-vivo QA in MRGRT: 3D EPID dosimetry for the Unity MR-linac*. Retrieved from https://hdl.handle.net/1887/136754

Version:	Publisher's Version
License:	Licence agreement concerning inclusion of doctoral thesis in the Institutional Repository of the University of Leiden
Downloaded from:	https://hdl.handle.net/1887/136754

Note: To cite this publication please use the final published version (if applicable).

Cover Page

Universiteit Leiden

Leiden University Repository

The handle http://hdl.handle.net/1887/136754 holds various files of this Leiden University dissertation.

Author: Torres Xirau, I.
Title: Patient-specific in-vivo QA in MRGRT: 3D EPID dosimetry for the Unity MR-linac
Issue Date: 2020-09-15

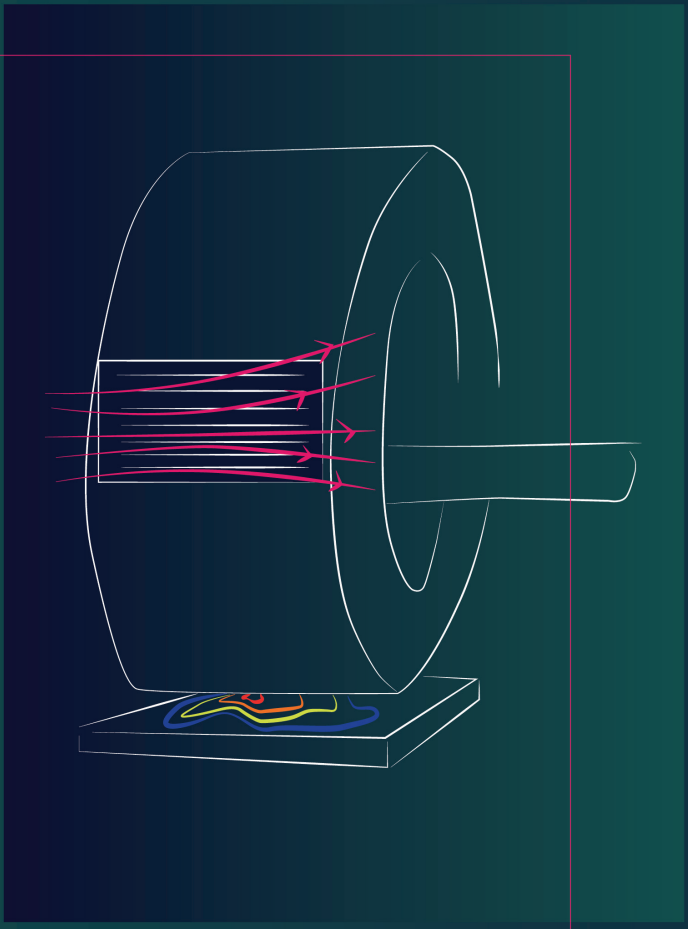

4.

TWO DIMENSIONAL EPID DOSIMETRY FOR AN MR-LINAC: PROOF OF CONCEPT.

Iban Torres-Xirau
Igor Olaciregui-Ruiz
Uulke A. van der Heide
Anton Mans

Department of Radiation Oncology,
The Netherlands Cancer Institute–Antoni van Leeuwenhoek Hospital,
Plesmanlaan 121, 1066 CX Amsterdam, The Netherlands

Medical Physics, Volume 46, Number 9, Pages 4193-4203
Published September 2019 • *© 2019 American Association of Physicists in Medicine*

Abstract

At our institute, *in-vivo* patient dose distributions are reconstructed for all treatments delivered using conventional linacs from Electronic Portal Imaging Device (EPID) transit images acquired during treatment using a simple back-projection model. Currently, the clinical implementation of MRI-guided radiotherapy systems, which aims for online and real-time adaptation of the treatment plan, is progressing. In our department the MR-linac (Unity, Elekta AB, Stockholm, Sweden) is now in clinical use. The aim of this work is to demonstrate the feasibility of 2D EPID dosimetric verification for the MR-linac by comparing back-projected EPID doses to ionization chamber (IC) array dose distributions.

Our conventional back projection algorithm was adapted for the MR-linac. The most important changes involve modeling of the attenuation by and scatter from the cryostat. The commissioning process involved the acquisition of square field EPID measurements using various phantom setups (varying SSD, phantom thickness and field size). Commissioning models were created for gantry 0, 90 and 180 degrees and verified by comparing EPID reconstructed 2D dose distributions to measurements made with the OCTAVIUS 1500 IC array (PTW, Freiburg, Germany) for 2 prostate and 1 rectum IMRT plans (25 beams total). The average of the γ parameters (γ-mean and γ-pass rate) and the dose difference at a reference point were reported. Due to their construction, the attenuation of couch, bridge and cryostat shows a much stronger dependence on gantry angle in the MR-linac compared to conventional linacs. We present a method to correct for these effects. This method is validated by dose reconstruction of the 25 IMRT beams recorded at a certain gantry angle using the model of another gantry angle, combined with the correction method.

For dose verification performed at a gantry angle identical to the

commissioned model the average y-mean and y-pass rate values (3% global dose, 2 mm, 10% isodose) were 0.37 ± 0.07 and 98.1, 95% CI [98.1 ± 2.4], respectively. The average dose difference at the reference point was -0.5% ± 1.8%. Verification at gantry angles different from the commissioned model (i.e., using the gantry angle dependent correction) reported 0.39 ± 0.08 and 97.6, 95% CI [96.9, 98.3] average y-mean and y-pass rate values. The average dose difference at the reference point was: -0.1% ± 1.8%.

The EPID dosimetry back projection model was successfully adapted for the MR-linac at gantry 0°, 90° and 180°, accounting for the presence of the MRI housing between phantom (or patient) and the EPID. A method to account for the gantry angle dependence was also tested reporting similar results.

Keywords: EPID, portal dosimetry, dose verification, MR-linac, QA, Unity.

4.1. Introduction

Although Electronic portal imaging devices (EPIDs) were originally designed for patient position verification, their use for dosimetric applications has been acknowledged both for pre-treatment and *in vivo* dose verification. The dose-response characteristics of amorphous silicon (a-Si) EPIDs have been broadly studied [113,114,119,138,140–143] and several EPID based solutions are being used both for intensity-modulated radiation therapy (IMRT) [24,58,60,144–147] and VMAT [57,59,148–150] treatments.

Recently, treatment machines combining a radiation source with an MRI system have been developed and are clinically used. In our department, the MR-linac (Unity, Elekta AB, Stockholm, Sweden) [92,151] has been installed and patient treatments have started. The system is equipped with an EPID mounted on the rotating gantry, opposite to the accelerator head, allowing for simultaneous beam irradiation, EPID acquisition and MR imaging [93].

Online adaptive strategies in MRIgRT will become clinically feasible [94] as result of the ongoing developments in fast re-contouring and re-planning. In this context, independent tools for the verification of these adaptive treatments will become imperative. Existing pre-treatment tools for QA in the MR-linac are typically time-consuming solutions which, besides, are not applicable for an online adaptive workflow [97–100]. Alternative patient-specific QA solutions have been proposed, such as fast sanity checks on the adapted plan [101], in-vivo geometrical accuracy of the delivery using EPID images [152], or the use of independent calculations fed with linac log files [76,153–155].

An MR-only workflow would allow for MRI-based delineation while performing dose calculation on a synthetic CT derived from that MRI study. The use of log files in combination with an independent dose calculation algorithm using the synthetic CT is an alternative treatment verification method. However, this approach relies on the correctness

of the log files [105] and synthetic CT, and independent dose algorithms that consider the magnetic field are not widely available.
Currently, in all institutions that have started treating patients on the MR-linac, the dosimetric verification of adapted plans if performed is done after the treatment fraction using a detector array or film in combination with a phantom. The use of transit EPID dosimetry provides a complementary solution to these methods, able to perform an independent end-to-end check of the entire chain, verifying data transfer, dose delivery, patient set-up, MLC calibration and dose calculation [105], and also synthetic CT determination. Moreover, the EPID is already attached to the machine, and allows for automation and even in real-time treatment verification [89,133]. However, it also comes with limitations given the position of the panel with respect to the beam, and when used without taking the magnetic field into account in the back-projection dose engine.
We have shown the dosimetric characteristics of the EPID to be similar in the MR-linac compared to conventional linacs [156]. Furthermore, the magnetic field at the EPID location is very low (the time-varying component during imaging even lower) and has been demonstrated not to influence the EPID images [156]. This suggests feasibility of the adaptation of existing back-projection models to the MR-linac geometry. The feasibility of correcting EPID images for the presence of extra scattering and attenuating material between phantom and EPID has also been demonstrated [139]. The aim of this study is to bring all these prior results together, and demonstrate the feasibility of back-projection EPID dosimetry for the MR-linac by comparing 2D EPID reconstructed dose distributions to absolute dose measurements in a phantom.

4.2. Materials and Methods

4.2.1 Accelerator, EPID, acquisition software and measuring equipment.

The MR-linac system combines a 7 MV flattening filter free (FFF) beam linac (Elekta AB, Stockholm, Sweden) with an integrated wide bore 1.5 T MRI scanner (Philips Medical Systems, Best, the Netherlands). The MR-linac uses an Elekta Agility-based multi-leaf collimator (MLC) consisting of 160 leaves with a projected width of a single leaf of 0.72 cm at the isocenter plane.

The accelerator and EPID are mounted on a ring gantry built around the MRI scanner. The source-to-isocenter distance is 143.5 cm, and the source-to-detector distance (SDD) is fixed to 265.3 cm, resulting in a magnification factor of 1.84. The central region of the magnet is free of gradient coils and shimming hardware, allowing for minimal and homogenous attenuation of the beam by the cryostat. This region determines the maximum allowed field size in the longitudinal direction (±11 cm at isocenter). The effective size of the beam exiting the MRI scanner is larger due to divergence, limiting the EPID acquisition of un-attenuated beams to an irradiation field of a maximum of ±4.8 cm in each direction of the longitudinal axis at the isocenter. For larger fields, the exit beam's dimensions exceed the coil-free region and therefore, the exit beam is inhomogeneously attenuated. Moreover, due to the non-centered position of the EPID with respect to the beam axis, fields exceeding 8 cm in the positive longitudinal axis are not entirely captured by the EPID. **Figure 4.1** illustrates the EPID position in the MR-linac geometry and the characteristics of acquired images. Therefore, in this study the reconstructed dose distributions are truncated at ± 5.6 cm, close to the border of the area of homogenous attenuation.

Due to the rigid ring gantry on the Unity system, the EPID sag is smaller than in conventional linacs. On our system, the isocenter position on the panel was determined to be stable within 0.5 mm, which we considered negligible to our purposes. The Elekta iViewGT panel is an a-Si flat panel X-ray detector (XRD 1642 AP, Perkin Elmer Optoelectronics, Wiesbaden, Germany) with a 41x41 cm^2 detection area (1024x1024 pixels), and a pixel pitch of 0.4 mm. Images were acquired using Elekta's MVIC software. Array measurements were performed using an MR-compatible OCTAVIUS 1500 2D detector array (PTW, Freiburg, Germany), having 1405 vented ICs with 7.1 mm center-to-center distance, with an uncertainty of ±0.5%, which was cross-calibrated to a known value for a reference beam.

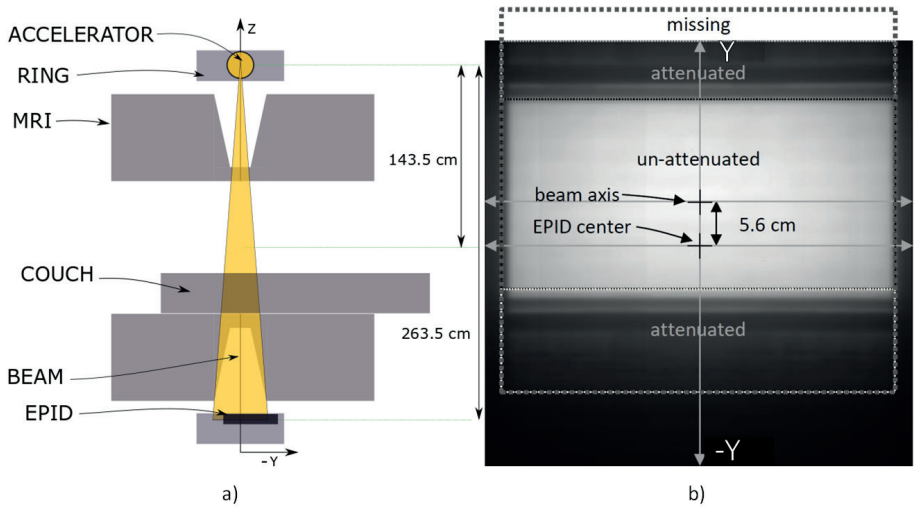

Figure 4.1: a) MR-linac cross-section. In the Y direction, the beam center is not aligned with the center of the EPID. Therefore, parts of large fields fall outside the EPID detection area. **b**) EPID image of a 20 × 20 cm^2 (FFF) beam. The centers of the EPID and the beam are marked with a cross and a dashed line shows the entire square shape of the field arriving to the EPID, which the EPID receives in un-attenuated parts (like in conventional linacs), attenuated parts, and missing parts.

4.2.2. Back-projection algorithm for the MR linac

4.2.2.1. Rationale

The conventional back-projection algorithm requires the portal dose distribution at the EPID level, the transmission through the phantom (or patient) and the geometry of the phantom (or patient). For the determination of the portal dose distribution at the EPID level, the parameters of our algorithm are fitted against IC dose measurements performed at the level of the EPID. Such measurements are made by an IC inside a cylindrical miniphantom at the location of the EPID [58,70]. This is impossible in the MR-linac due to the location of the panel, as there is no physical space to execute such measurements. Therefore, similar measurements were made at the isocenter and rescaled to the EPID level using the inverse square law (ISQL), to be used as surrogate for measurements at position of the EPID in the absence of the cryostat. The purpose of these adaptations to the back-projection algorithm is to estimate the attenuation and scatter sensed by the EPID, generated by the cryostat, couch and bridge. Using this result, the primary dose at the EPID level can be determined. Effectively, the adapted algorithm removes the influence of the cryostat and the intrinsic scatter generated within the EPID in the conversion from pixel values to portal dose distributions at EPID level. The other parts of the back-projection algorithm are not modified.

4.2.2.2 IC array measurements

The array is used in two configurations. First, to measure dose at d_{max} (with 13 mm of buildup) at isocenter as a surrogate for dose measurements in the miniphantom for conventional linacs. Second, for measurements at 10 cm depth, the detector array is placed at 10 cm from surface of a 23 cm slab phantom, since the couch of the MR-linac does not allow for vertical motion and the isocenter lies at 13 cm above the couch.

4.2.2.3. Image processing

All acquired EPID images are pre-processed into the PV_{ij}^{proc}, which is the time-integrated pixel value EPID image corrected for the dark field, the flood field and for bad pixels [119], and shifted 5.6 cm in the Y-direction to compensate for the off-axis alignment of the panel with respect to the beam [156].

4.2.2.4. Sij Matrix

The Sij matrix is a correction directly applied to each PV_{ij}^{proc} image to compensate for pixel sensitivity variations and off-axis differential photon energy [46]. Note that in MR-linac case, the Sij matrix is also influenced by the attenuation of the beam through the MRI scanner between isocenter and EPID. The Sij matrix is defined as follows:

$$S_{ij} = \frac{OCT_{ij}^{ISO \rightarrow EPID,22x22}}{PV_{ij}^{proc,22x22}} \quad (1)$$

where OCT is the measurement of a large field (22x22 cm^2) by the OCTAVIUS 1500 detector array at d_{max} positioned at isocenter and scaled to EPID level (using the ISQL). $PV_{ij}^{proc,22x22}$ is the corresponding EPID image after processing. The OCTAVIUS 2D array field was bi-linearly interpolated and later a uniform smoothing over a 5x5 pixel neighborhood was performed to achieve the spatial resolution of the EPID.

4.2.2.5 Determination of the portal dose

Ideally, the conversion from pixel values to dose should be linear. The dose response D_r is defined as the ratio between the central region pixels and their corresponding dose measurement. The resulting image is called dose image:

$$D_{ij}^{EPID} = PV_{ij}^{proc} \cdot S_{ij} \cdot Dr \quad (2)$$

Note that the Sij matrix was obtained with measurements performed with a large field (22x22cm^2), so the dose image corresponds to the measured portal dose distribution only for this field size. However, the component of scatter from the MRI scanner towards the EPID, $Sc_{ij}^{MRI\rightarrow EPID}$ and the component of lateral scatter within the EPID, Sc_{ij}^{EPID} , are field size dependent. Hence, for any arbitrary field size, the dose image can be expressed as:

$$D_{ij}^{EPID} = PD_{ij}^{EPID\prime} + Sc_{ij}^{MRI\rightarrow EPID} + Sc_{ij}^{EPID}, \quad (3)$$

where $PD_{ij}^{EPID\prime}$ is the portal dose distribution measured for an arbitrary field size, without the extra effects of the cryostat, couch and bridge, and the scatter of the EPID. The scatter from the MRI towards the EPID is modeled as a convolution between the dose image D_{ij}^{EPID} and a scatter kernel $K_{ij}^{MRI\rightarrow EPID}$. Simultaneously, the scatter occurring within the EPID Sc_{ij}^{EPID}, is modeled as a deconvolution between the resulting dose image D_{ij}^{EPID} minus the scatter from the MRI to the EPID, and a scatter kernel K_{ij}^{EPID}:

$$Sc_{ij}^{MRI\rightarrow EPID} = D_{ij}^{EPID} \otimes K_{ij}^{MRI} \quad (4)$$

$$Sc_{ij}^{EPID} = (D_{ij}^{EPID} - Sc_{ij}^{MRI\rightarrow EPID}) \otimes^{-1} K_{ij}^{EPID} \quad (5)$$

As kernels we use a Gaussian filter for $K_{ij}^{MRI\rightarrow EPID}$ and the kernel suggested in [70] for the K_{ij}^{EPID}:

$$K_{ij}^{MRI} = \frac{c_{MRI}}{2\pi\sigma_{MRI}^2} \exp\left(-\frac{r_{ij}^2}{2\sigma_{MRI}^2}\right) \quad (6)$$

$$K_{ij}^{EPID} = c_{DR} \begin{cases} c_1 \cdot \frac{e^{-\mu \cdot r_{ij}}}{r_{ij}^2} & \text{for } r_{ij} \neq 0 \\ 1 & \text{for } r_{ij} = 0 \end{cases}, , \quad (7)$$

,

Where r_{ij} is the distance of a pixel ij from the central axis and c_{MRI}, σ_{MRI}^2, c_{DR}, c_1 and μ are the kernel parameters. The portal dose in (**3**) is then calculated as:

$$PD_{ij}^{EPID\prime} = D_{ij}^{EPID} - (D_{ij}^{EPID} \otimes K_{ij}^{MRI \to EPID}) - (D_{ij}^{EPID} - (D_{ij}^{EPID} \otimes K_{ij}^{MRI \to EPID})) \otimes^{-1} K_{ij}^{EPID} \quad (8)$$

Which is a function of the dose response Dr, and the parameters that determine the kernels K_{ij}^{EPID} and K_{ij}^{MRI} as expressed by:

$$PD_{ij}^{EPID\prime}(Dr, \sigma_{MRI}^2, c_{MRI}, c_{DR}, c_{1,} \mu) \quad (9)$$

The values of these model parameters are determined by a parametric fit of on-axis EPID-reconstructed dose values and the corresponding array measurements, for a set of field sizes (2x2 – 22x22 cm^2). For an accurate description of the portal dose image over the entire field of view, a 2D fitting procedure is finally introduced to minimize the difference in profiles of PD_{ij}^{EPID} images and array measurements. The corrected dose image PD_{ij}^{EPID} is defined as the dose image, PD_{ij}^{EPID} convolved with a kernel, K_{ij}^{prof}:

$$PD_{ij}^{EPID} = PD_{ij}^{EPID\prime} \otimes K_{ij}^{prof}, , \quad (10)$$

K_{ij}^{prof} is defined as a Gaussian kernel:

4

$$K_{ij}^{prof} = \frac{c_{prof}}{2\pi\sigma_{prof}^2} \exp\left(-\frac{r_{ij}^2}{2\sigma_{prof}^2}\right), \quad (11)$$

In order to determine the optimal σ_{prof}^2 and c_{prof} parameters of, K_{ij}^{prof}, the Euclidian distance between EPID and normalized measured profiles was minimized for all field sizes.

4.2.2.6 Final steps

After the portal dose image is calculated, the next steps of the adapted back-projection algorithm are identical to the conventional model: the portal dose is used to calculate the primary transmission using portal images with and without the phantom (or patient) in the beam. The primary dose within the phantom, Pr, is weighted with the Scatter-to-Primary Ratio (SPR) determined under reference conditions, $SPRr_{ref}$, which accounts for the thickness dependence of the scatter. The SPR is parametrized as a function of the primary transmission, the thickness of the patient and the depth of the reconstruction plane. Next, the result is convolved with the scatter kernel $Kmid_{ij}$, accounting for the field size dependence of the scatter in the reconstruction plane.

4.2.3. Full commissioning at gantries 0°,90°,180°

In our back-projection algorithm for conventional linacs, all gantry angles are equivalent in terms of EPID pixel conversion to dose. Hence, the parameters of the back-projection model are commissioned using measurements performed at gantry 0°, which are applied for all gantry angles. The only gantry angle dependent factor in the model is the correction for the attenuation of the couch top at the exit side of the patient. This is accounted for by a 2D couch attenuation model [157]. In the MR-linac geometry, however, the attenuation of the cryostat, couch and bridge (at the exit side of the phantom) varies considerably with

gantry angle. Ideally, the commissioning of the back-projection model would be performed for each possible gantry angle. However, as a gantry-mounted detector setup is not feasible within a slab phantom in the MR-linac, the commissioning process can only be carried out when the detector is perpendicular to the radiation beam, that is for gantry angles of 0°, 90°, 180° and 270°. Because of symmetry on the set-up, gantry angle 270 was omitted from this study. The set of measurements required for the full commissioning of our model is summarized in **Table 4.1**.

Table 4.1: Set of absolute dose measurements needed for the EPID back-projection model commissioning in the MR-linac geometry. Note that an EPID image needs to be acquired for each of these measurements.

Measurement	**Comment**	**Equipment**	**Phantom (cm^3)**	**Field Size (cm^2)**
1. S_{ij} matrix	To measure the relative sensitivity over the entire EPID and the 2D transmission through the MRI scanner	OCTAVIUS 1500 array at d_{max}		22x22
2. Field size series	No phantom, varying field size	OCTAVIUS 1500 array at d_{max}		2x2-20x20
3. Phantom series	Constant phantom thickness, varying field size	OCTAVIUS 1500 array at isocenter in slab phantom	30x30x20	2x2-20x20
4. Thickness series	Constant field size, varying phantom thickness	OCTAVIUS 1500 array at isocenter in slab phantom	30x30x 4-32	10x10

5. Gantry Angle Corr.	Large field at every gantry angle.	OCTAVIUS 1500 array at d_{max}	22x22

4.2.4. IMRT plans validation at gantries 0°, 90°, 180°:

At the time of this study, we chose patient categories that were likely to be treated first on the MR-linac. 3 plans (2 prostate and 1 rectum) were used, with around 1000 MU each, consisting of 25 beams (9, 9 and 7 respectively) ranging from 5 to 20 segments per beam, with a largest irradiated segment per plan of 48 cm^2 to 280 cm^2 were irradiated to a 23 cm slab phantom at the three gantry angles (0°, 90° and 180°). Additionally, the 2D detector array was used to measure dose distributions at the isocenter level at 10 cm depth. The EPID images were back-projected to the isocenter plane using the adapted back-projection algorithm commissioned at the corresponding gantry angle. 2D γ analysis (3% global, 2mm at 10% isodose) was performed between the detector array and EPID reconstructed dose distributions. The reference point was determined as the point with the lowest gradient within the points with dose value equal to or greater than 80% of the maximum in the measured dose.

4.2.5. Gantry angle correction

A method was introduced to adapt the commissioning model for use at arbitrary gantry angles. This approach assumes that the differences between the different gantry configurations affect the Sij matrix and the dose response. The modification of the S_{ij} Matrix is given by:

$$Sij_{ij}^{\mathrm{CGA}\rightarrow\mathrm{AGA}} = Sij_{ij}^{CGA}\frac{PV_{ij}^{proc,22x22,\mathrm{CGA}}}{PV_{ij}^{proc,22x22,\mathrm{AGA}}}\frac{OCT_{ij}^{ISO\rightarrow EPID,22x22,\mathrm{AGA}}}{OCT_{ij}^{ISO\rightarrow EPID,22x22,\mathrm{CGA}}} \quad (12)$$

Where Sij_{ij}^{CGA} is the Sij matrix obtained at a commissioned gantry angle (CGA, i.e., 0°, 90° or 180°) and $PV_{ij}^{proc,22x22,\mathrm{CGA}}$ and $PV_{ij}^{proc,22x22,GAC}$ correspond to the pre-processed open images of a 22x22 cm^2 field at a CGA and at an arbitrary gantry angle (AGA), respectively. $OCT_{ij}^{ISO\rightarrow EPID,22x22,\mathrm{CGA}}$ and $OCT_{ij}^{ISO\rightarrow EPID,22x22,AGA}$ are the 2D array measurements at isocenter at d_{max} for a 22x22 cm^2 field, scaled to the EPID level, both at CGA and AGA, respectively. Note that this correction requires the acquisition of an EPID image and a 2D array measurement of a large field (e.g. 22x22 cm^2) for each clinically relevant gantry angle, as included in **Table 1**. However, since in this study the validation of the method could only be performed with the 2D array positioned perpendicular to the beam, only data for gantries 0, 90 and 180 was acquired.

A normalization factor is applied to account for the differences in transmission leading to different dose response. Therefore, the dose response Dr is modified to fit the central region of a back-projected EPID image of a 10x10 cm^2 field irradiated to a slab phantom and back-projected to the isocenter at 10 cm depth, $\langle D_{ij}^{mid,10x10}\rangle_{Roi}^{\mathrm{CGA}}$, to the dose measured with the array, $\langle OCT_{ij}^{10x10}\rangle_{Roi}^{AGA}$.

$$N^{AGA} = \frac{\langle D_{ij}^{mid,10x10}\rangle_{Roi}^{\mathrm{CGA}}}{\langle OCT_{ij}^{10x10}\rangle_{Roi}^{AGA}} \quad (14)$$

The adapted Dose response is defined as:

$$Dr^{\mathrm{CGA}\rightarrow AGA} = Dr^{\mathrm{CGA}}\, N^{AGA} \quad (15)$$

Where Dr^{CGA} is the dose response of the commissioned gantry angle, and N^{AGA} is the normalization factor.

4

4.2.6. Validation of adaptation to arbitrary gantry angles

To validate this approach, a full commissioning of the cardinal gantry angles was performed first, and three models were created. For each of the three models, the gantry angle correction can be applied. EPID images of IMRT fields irradiated at gantry 90° were back-projected using the model commissioned at gantry 0°, EPID images irradiated at gantry 180° were back-projected using the model commissioned at gantry 90° and EPID images acquired at gantry 0° were back-projected using the model of gantry 180°. The back-projected 2D dose distributions of the 25 IMRT beams were compared to the original array measurements of gantry angles 90° and 180° and 0°, respectively.

4.3. Results

4.3.1. Validation of the algorithm

The performance of $K_{ij}^{MRI\rightarrow EPID}$, K_{ij}^{EPID} and K_{ij}^{prof}, which correct for the presence of scatter at the EPID level, can be seen in **Figure 4.2**, where EPID measured output factors before and after fitting to the IC measurements at isocenter, are shown. **Figure 4.3** presents the normalized EPID X profiles before and after applying the scatter kernels K_{ij}^{prof}, K_{ij}^{EPID} and $K_{ij}^{MRI\rightarrow EPID}$, compared to the measured dose profile with the detector array at isocenter at d_{max}, after scaling to the EPID level.

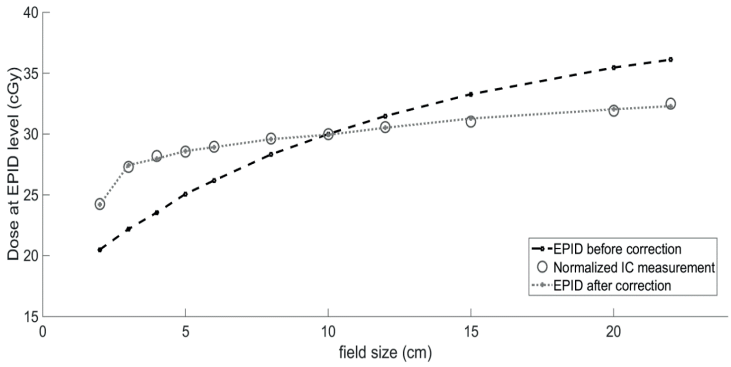

Figure 4.2: Output factors measured with the 1500 OCTAVIUS detector array, (open circles) and EPID (lines). The normalized central pixel dose of the EPID before scatter correction is plotted in dashed black. After applying the scatter kernels K_{ij}^{EPID} and K_{ij}^{MRI}, the EPID signal corrected for the scatter is derived (dotted grey line). Note that due to possible small misalignments, to the spatial resolution of the detector used in this study (1500 OCTAVIUS array) and the size of the ionization chambers, for small fields (e.g. 2x2 cm^2) the measured dose on-axis might be underestimated.

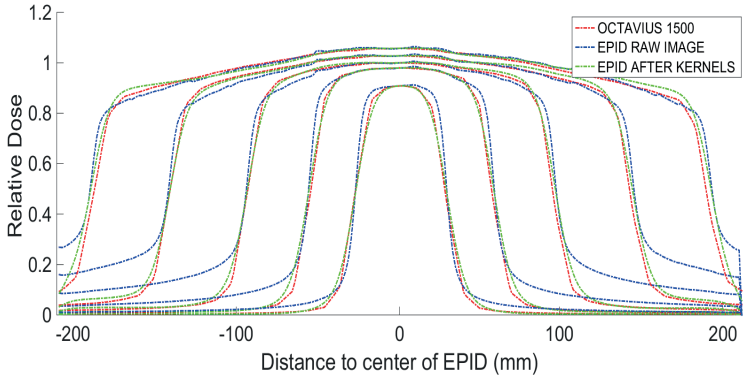

Figure 4.3: X profiles of the raw (dashed blue) and after convolving with the scatter kernels (dashed green) EPID images for 3x3, 5x5, 10x10, 15x15 and 20x20 cm2 square fields, compared to the profiles measured with the OCTAVIUS 1500 array (red).

4.3.2. IMRT beams at gantries 0°, 90° and 180°

25 IMRT fields from three treatments (2 prostate, 1 rectum) were verified for the three commissioned gantry angles. An arbitrary subset of γ maps

of these fields comparing detector array and EPID reconstructed dose distributions is shown in **Figure 4.4. Table 4.2** reports the average and standard deviation of three parameters: γ-mean, γ-pass rate and dose difference at the reference point ($\Delta Dose_{RP}$).

Table 4.2: Averaged γ results and dose difference at a reference point for 25 IMRT fields at gantry 0°, 90° and 180°.

Gantry angle	$\langle \gamma_{mean} \rangle$	$\langle$ **Passrate** $\%_{\gamma<1}$ $\rangle$	$\langle \Delta Dose_{RP} \rangle$
0	0.37± 0.07	97.9, 95% CI [96.7, 99.1]	-0.8% ± 1.8%
90	0.36± 0.09	98.1, 95% CI [97,5, 99,3]	-0.3% ± 1.9%
180	0.37± 0.06	97.9, 95% CI [97.2, 98.7]	-0.5% ± 1.7%

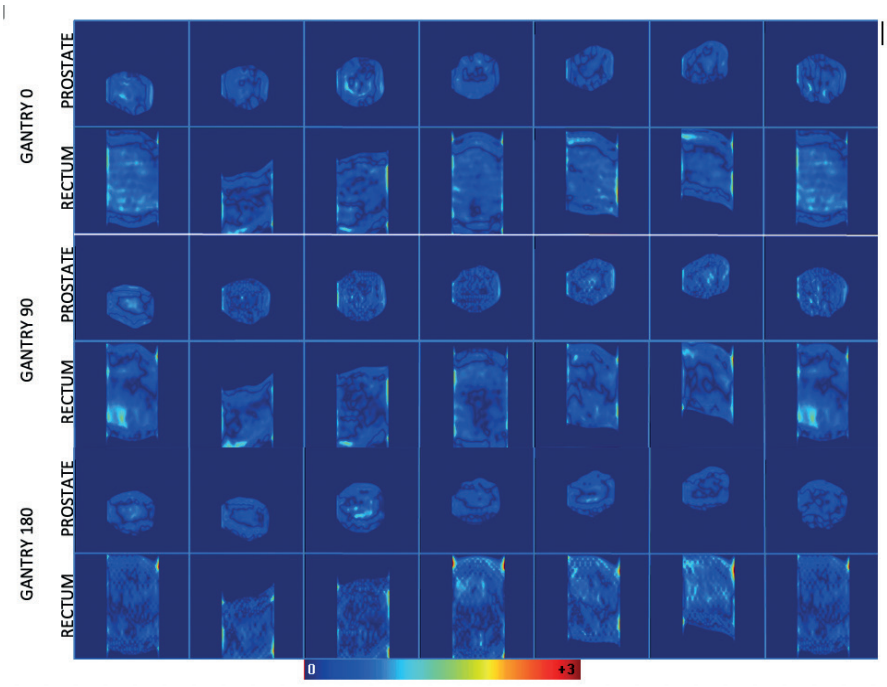

Figure 4.4: The first 2 rows show a random subset of γ maps (3%, 2mm, global 10% isodose) for 7 prostate plans and 7 rectum plans irradiated at gantry 0°. Rows 3 and 4 show the γ maps for the same rectum and prostate plans irradiated at 90° degrees. The last two rows are the γ maps for the same fields irradiated at and 180°.

A sample of X and Y profiles of both EPID and array measured dose distributions at gantries 0°, 90° and 180° is presented in **Figure 4.5**, where the reference point is also indicated for each image.

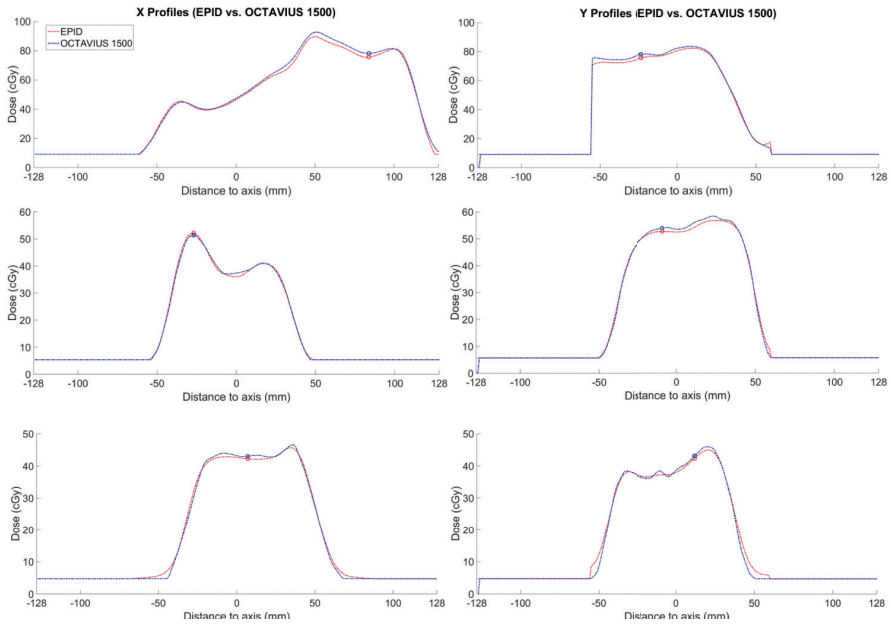

Figure 4.5: X (left) and Y (right) EPID and measured array profiles for one prostate IMRT field (first row) and two rectum (second and third rows) IMRT fields irradiated at gantry angles 0° (first row), 90° (second row) and 180° (third row). EPID profiles are plotted in dashed red and array profiles in dashed blue. The blue and red circles determine the reference point were the dose difference was calculated. Note in the Y profile of the prostate beam, that the signal of both EPID and array measured dose distributions were truncated at ±5.6 cm.

4.3.3. Gantry angle dependency validation

The same EPID images acquired for the 25 IMRT fields at three gantry angles were used to validate the gantry angle correction method. The 25 images acquired at gantry angle 90° were back-projected using the model commissioned at gantry angle 0. Similarly, EPID images acquired at gantry angle 180° were back-projected using the model of

gantry angle 90° and EPID images acquired at gantry angle 0° were back-projected using the model of gantry angle 180°. Dose difference at reference point and γ results are reported for the comparison to detector array measurements. **Figure 4.6** shows the γ maps for the same fields as in **Figure 4.4**, in this case using the gantry angle correction. **Table 4.3** reports the averaged γ-mean and γ-pass rate together with the dose difference at a reference point ($\Delta\mathrm{Dose}_{RP}$).

Table 4.3: Average γ results and dose difference at a reference point for 25 IMRT fields acquired at gantry 0°, 90° and 180°, using the gantry adaptation solution and the models of gantries 180°, 0° and 90° as a baseline, respectively.

Measurement / model gantry angle	$\langle \gamma_{mean} \rangle$	$\langle \mathrm{Passrate}\ \%_{\gamma<1} \rangle$	$\langle \Delta\mathrm{Dose}_{RP} \rangle$
0° / 180°	0.39± 0.07	97.9, 95% CI [97.7, 99.0]	-0.5% ± 2.1%
90° / 0°	0.37± 0.08	98.4, 95% CI [97.3, 98.9]	-0.3% ± 1.8%
180° / 90°	0.39± 0.07	97.9, 95% CI [96.5, 98.3]	0.5% ± 1.7%

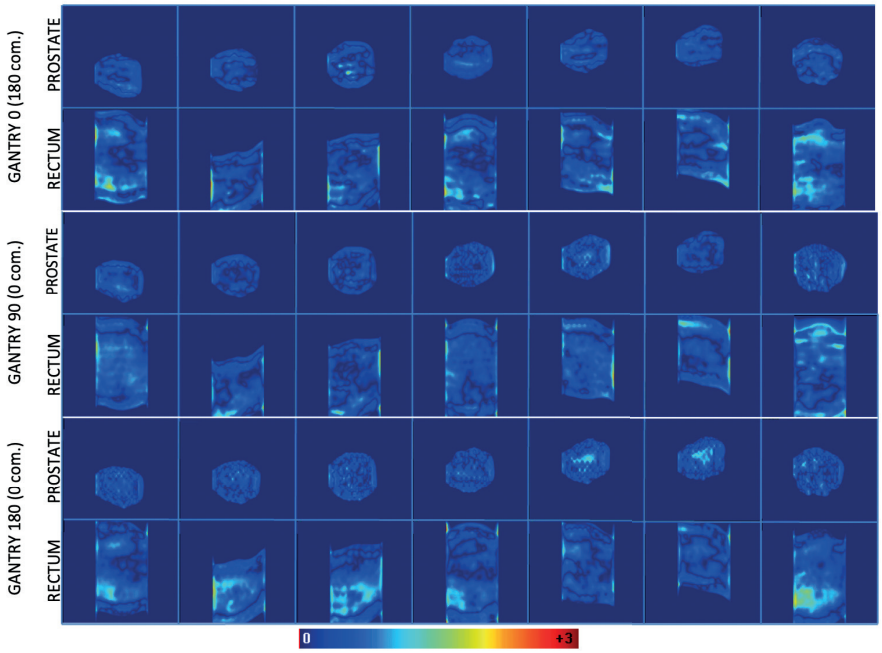

Figure 4.6: The first 2 rows show a subset of γ maps (3%, 2mm, global 10% isodose) for 7 prostate plans and 7 rectum plans irradiated at gantry 0° and reconstructed using the gantry angle correction from 180→0. Rows 3 and 4 show the γ maps for the same rectum and prostate plans irradiated at 90 degrees and reconstructed using the correction 0→90. The last two rows are the γ maps for the same fields irradiated at and 180 degrees and reconstructed using the correction 90→180.

4.4. Discussion

We successfully adapted our EPID dosimetry back-projection algorithm to the MR-linac geometry. Comparison of EPID reconstructed and IC measured 2D dose distributions at isocenter level show good correspondence. This proof of concept study demonstrates that for three cardinal gantry angles, the algorithm is able to reconstruct the dose distribution inside a slab phantom accurately. Furthermore, a method is introduced to correct for the gantry angle dependent

attenuation of the cryostat, couch and bridge, and was validated for gantry angles 0°, 90° and 180°. Validation of this correction for arbitrary angles is beyond the scope of present work, as it involves IC array measurements that, with our current equipment, can only be performed at the cardinal angles. In future work, when expanding the method to all gantry angles, attenuation of the couch, bridge and the cryostat pipe will have to be taken into account in the back-projection algorithm. A method to correct for the influence of these structures will have to be developed and tested and the accuracy of such a method will have to be assessed.

The results presented in Table 4.2 suggest a minor underdosage in EPID reconstructed dose. This can also be observed in some of the graphs in Figure 4.5. To further determine whether this underdosage is systematic or not, more data would be required. An estimate of the uncertainty, obtained from the standard deviation of the reconstruction point doses of the 25 IMRT fields (Table 2 and 3), is 2% (1 SD).

The comparison between the EPID reconstructed and IC array measured dose distributions disregard any possible dose re-distributions caused by the magnetic field inside the phantom due to the electron return effect (ERE). Our algorithm at this stage does not account for these effects. In this work, however, no inhomogeneities are present in the phantom geometry. And given the spatial resolution of the Octavius 2D array, we expect the impact of these effects to be negligible. Moreover, no skewness was observed in the Sij matrix. Furthermore, the EPID measurements were fitted to array measurements performed in a 1.5T B-field and the EPID reconstructed dose was compared to dose distributions measured in a 1.5T B-field, both showing good agreement.

In the patient geometry, however, the ERE might lead to important dose redistributions. So, it is expected that for EPID in vivo dosimetry

the current solution will fall short. EPID dosimetry can be a valuable tool for the detection of gross errors in the patient and for the detection of smaller deviations in situations where the effect of ERE is small. For instance, virtual in air EPID measurements [88] can be used to reconstruct EPID dose distributions to a phantom anatomy, instead of OCTAVIUS measurements which are more cumbersome by nature.
Several solutions can be thought of to solve this problem. First is the comparison of the EPID back-projected dose distribution to a copy of the planned dose distribution calculated without the magnetic field (i.e., a 'non-magnet' solution, similarly to the 'in-aqua' concept used for verification of lung treatments [86]). Alternatively, the back-projection algorithm could be modified to reconstruct the fluence in a plane before the patient and use it as input for a Monte Carlo dose calculation which accounts for the magnetic field, which can then be compared to the planned dose distribution. These approaches would, however, imply the use of a dose calculation engine, which would hamper fast computations in the verification process. The chosen technique to solve this problem is out of the scope of this work.

As with our conventional algorithm, the parameters of the model are determined using water-based kernels and consequently, the model is expected to work most accurately for back-projection in homogeneous media (such as slab phantoms or the abdomen or pelvis. For dose verification in sites involving (large) tissue heterogeneities, e.g. lung, esophagus and breast, the same in aqua vivo approach as in the conventional algorithm can be used [86]. The performance of this approach will be assessed in future work

Only pelvic treatments were included in this study. However, we expect the performance of the adapted back-projection algorithm to be treatment site independent [90]. Validation of the method in clinical practice falls outside the scope of this study.

Another limitation when using the EPID for dosimetry in the MR-linac in the current setup is that parts of beams exceeding 8.1 cm in the cranial direction cannot be detected due to the non-centered position of the panel. As a result, for treatments with large fields parts of the reconstructed dose distribution will be missing, and cannot be verified. Due to the design of the MR-linac, alignment of the panel with the beam is not straightforward.

The extra attenuation of the beam by the cryostat outside the window ±5.6 cm in the longitudinal direction is another limitation of the MR-linac geometry and was not dealt with in current work. However, we are positive that the available signal in these strongly attenuated areas can be used for dosimetry purposes, although the accuracy of the final reconstructed dose distribution inside the phantom or patient will probably be lower. Overall, we observed that the verification of the treatments will be constrained by the size of the irradiated beams and therefore the accumulated EPID reconstructed dose distribution may not be not be possible for certain target volumes. In clinical practice this limitation does not play a role for prostate and all stereotactic treatments. For treatments with field sizes exceeding the aforementioned window, we anticipate a hybrid approach with highest accuracy in the central region, and lower accuracy in the peripheral area.

In this proof of concept, EPID-based dose reconstruction at the isocenter plane is presented as a QA tool for the MR-linac in 2D. Future work includes the adaptation of this method to allow for 3D dose reconstructions for any gantry angle and comparison to planned dose distributions.

4.5. Conclusions

Our EPID dosimetry back projection algorithm was successfully adapted for the MR-linac geometry, accounting for the presence of the MRI housing between phantom (or patient) and EPID. Both the attenuation of the cryostat and the scatter from the cryostat reaching the panel were successfully modelled. The algorithm was commissioned at three gantry angles: 0, 90 and 180 degrees. Excellent agreement was found for 25 IMRT beams between IC measured and EPID reconstructed 2D dose distributions in a phantom positioned at the isocenter. Moreover, a solution is presented for the gantry angle dependence of the attenuation of cryostat, couch and bridge. Validation of this method using data measured at a certain cardinal angle, but back-projected using the model from another angle, again showed excellent agreement. This work is an essential step towards an accurate and independent integrated dose verification tool for the MR-linac.

4.6. Disclosure of conflicts of interest

Support for this research was provided, in part, by Elekta AB, Stockholm, Sweden.

4.7. Acknowledgments

We would like to thank Jochem Kaas, Thijs Perik and Begoña Vivas for assistance with the measurements.